



Novel Volume-Improved Design Method of Large-Slenderness-Ratio Cone-Derived Waveriders

Ding Wang,* Jiang-Feng Wang,[†] Long-Fei Li,[‡] and Tian-Peng Yang[§]

Nanjing University of Aeronautics and Astronautics, 210016 Nanjing, People's Republic of China

and

Jiang-Tao Chen[¶]

China Aerodynamics Research and Development Center,
621000 Mianyang, People's Republic of China

<https://doi.org/10.2514/1.J059365>

A novel method is developed to improve the volume performance of large-slenderness-ratio cone-derived waveriders. Under the consideration of space utilization, loading capacity, and upper wall expansion performance, the design method is composed of an improved basic flowfield and a specially designed M-shaped flow capture curve. In addition, an improved evaluation method is proposed to provide a better measurement of volume performance for large-slenderness-ratio waveriders than the conventional method, which can also guide the design of volume-improved waveriders. The volume-improved waveriders and conventional cone-derived waveriders with slenderness ratios of more than nine are designed under the condition of a cruising altitude of 40 km and a Mach number of 12. After investigating their volume and aerodynamic performance, it can be found that the volume-improved waverider can achieve about a 48% volume increment, a 91% effective volume increment, and a four times larger volume growth rate compared to the conventional waverider. Furthermore, the lift-to-drag ratio of the volume-improved waverider is higher than that of the conventional waverider in the inviscid case, whereas it is smaller under the viscous condition. The gap in the viscous lift-to-drag ratio between the two waveriders reduces with the increasing attack of angle and is less than 8% at the design condition.

Nomenclature

C_d	= drag coefficient
C_l	= lift coefficient
G_{exp}^S and G_{exp}^V	= area growth rate of the i th cross section
L/D	= volume growth rate
Ma	= lift-to-drag ratio
M_∞	= Mach number
p_∞	= Mach number of freestream
$S_{\text{cb}-p}$	= static pressure of freestream
S_{eff}	= projected area of envelope box
S_{w-p}	= effective area of cross-sectional contour
$S_{w-\text{wet}}$	= projected area of waverider
T_∞	= wetted area of waverider
V_{eb}	= static temperature of freestream
V_{eff}	= volume of envelope box
V_w	= effective volume of waverider
$\text{VRT}_{\text{eff}/\text{eb}}$	= volume ratio defined as $V_{\text{eff}}/V_{\text{eb}}$
$\text{VRT}_{\text{eff}/w}$	= volume ratio defined as V_{eff}/V_w
$\text{VRT}_{w/\text{eb}}$	= volume ratio defined as V_w/V_{eb}
α	= angle of attack
$\eta_{\text{cb}-p}$	= volumetric efficiency with the projected area of envelope box
η_p	= volumetric efficiency with the projected area of waverider

$$\begin{aligned}\eta_{\text{wet}} &= \text{volumetric efficiency with the wetted area of waverider} \\ \rho_\infty &= \text{density of freestream}\end{aligned}$$

I. Introduction

A LARGE slenderness ratio is a common characteristic for hypersonic vehicles such as the X-43 [1], the X-51 [2], Advanced Hypersonic Weapon [3], etc., which puts forward a high requirement for the volume performance of the designed vehicle. Hence, although a waverider has a higher lift-to-drag ratio and better precompression ability than a slender body [4] or lifting body [3], its application is still seriously restricted in such cases due to the unsatisfactory volume performance. To better apply the waverider to the design of large-slenderness-ratio hypersonic vehicles, a design method of a volume-improved waverider needs to be developed.

The leading-edge region of the waverider generally needs to be thin enough to sustain good waverider characteristics, which leads to a special cross-sectional contour and a much less available volume than its geometrical volume. Consequently, an evaluation method for the volume performance is in strong demand. According to the geometrical characteristics of the waverider, the volumetric efficiency defined as $V_w^{2/3}/S_{w-\text{wet}}$ [5] or $V_w^{2/3}/S_{w-p}$ [6] was proposed to evaluate the space utilization, where V_w , $S_{w-\text{wet}}$, and S_{w-p} are the volume, wetted area, and projected area of the waverider, respectively. Although it is widely welcomed due to its simple definition and clear meaning [5–11], the volume efficiency still needs to be improved in the case of large-slenderness-ratio waveriders owing to three reasons. First, the increment of volume may be more likely less than the corresponding increment of the projected area or wetted area, and the volumetric efficiency is sensitive to the choice of the denominator. Hence, the valuable increment in volume may lead to a worse evaluation result. Second, the occupied area is generally determined by the design task and not a specific waverider, and it has only a weak relation with the wetted area and the projected area. Third, only part of the volume can be used to set loads due to the special cross-sectional contour of the waverider. What is more, the reasonable evaluations for loading capacity and upper wall expansion performance are also in strong demand. The evaluation method is of great significance for waveriders because it not only establishes the evaluation criterion but also guides the design of the volume-improved

Received 31 December 2019; revision received 4 May 2020; accepted for publication 15 June 2020; published online 29 September 2020. Copyright © 2020 by the American Institute of Aeronautics and Astronautics, Inc. All rights reserved. All requests for copying and permission to reprint should be submitted to CCC at www.copyright.com; employ the eISSN 1533-385X to initiate your request. See also AIAA Rights and Permissions www.aiaa.org/randp.

*Ph.D. Student, College of Aerospace Engineering; dingwang@nuaa.edu.cn.

[†]Professor, College of Aerospace Engineering; wangjf@nuaa.edu.cn (Corresponding Author).

[‡]Ph.D. Student, College of Aerospace Engineering; lf_li@nuaa.edu.cn.

[§]Ph.D. Student, College of Aerospace Engineering; yangtianpeng@nuaa.edu.cn.

[¶]Assistant Researcher; chenjt02@sina.cn.

waverider. Therefore, an improved evaluation method needs further study.

Over the past few decades, many waverider design methods have been developed, including the cone-derived method [12] (as shown in Fig. 1), the osculating cone method [13] (as shown in Fig. 2), the osculating axisymmetric flow method [14], the osculating flowfield method [15,16], etc. Among these, the cone-derived method has attracted a lot of research interests in the design of hypersonic cruising vehicles because of its excellent aerodynamic performance and simplicity of operation. The design frameworks of the methods mentioned earlier are similar and named the osculating framework for convenience of discussion. Under this framework, the design of the waverider mainly consists of the basic flowfield design and the spatial arrangement of the flowfield slices. Consequently, the volume performance of the waverider can be improved from these two points of view.

Under the osculating framework, the lower wall of the waverider is generated by tracing streamlines in the basic flowfield. Hence, the basic flowfield has an important influence on the volume performance of the waverider. Yu et al. [5] explored the inverse design method of the basic flowfield with an arbitrarily shaped shock wave. They found that the waverider based on the convex shock wave can considerably increase the lift coefficient and lift-to-drag ratio while decreasing the drag coefficient and volumetric efficiency. Liu et al. [17] investigated the influence of wall pressure distribution of the basic flowfield. Their results showed that the increasing wall pressure leads to a larger volume and lower lift-to-drag ratio. Recently, in order to improve the aerodynamic performance over a wide range of speeds, a class of spanwise-variable-parameter waveriders was proposed where the design parameters of the basic flowfield in each osculating plane are variable. The lower wall of the waverider in each osculating plane changes correspondingly. Liu et al. [10] designed a spanwise variable shock angle waverider. They found that the waverider with a spanwise increasing shock angle has a larger volume and lower lift-to-drag ratio. The spanwise variable Mach number waveriders [18,19] are also similar. On the other hand, most the inner space of the waverider locates at its aft section which can be effectively extended by extending the basic flowfield. Considering that the basic flowfield of the waverider inlet can be regarded as an extension of the basic flowfield of the waverider, it can be used to improve the volume

performance of the waverider. Matthews and Jones [20] designed a waverider inlet basic flowfield with constant pressure distribution that extends the compression zone of the waverider basic flowfield and adds a reflected shock. Drayna et al. [21] developed a truncated Busemann basic flowfield that balances the skin friction and shock losses. Wang et al. [22] integrated the multistage compression cone and the Busemann flowfield, which has a smaller drag coefficient and higher lift-to-drag ratio. Barkmeyer et al. [23] designed an inverted nozzle basic flowfield. You et al. [24] designed a novel basic flowfield named ICFC (which stands for internal conical flow "C") by integrating ICFA (which stands for internal conical flow "A" [25]) with the truncated Busemann flowfield, which can receive a conical impinging shock at the entrance and generate a relatively uniform flow. Yu et al. [26] and Huang et al. [27] developed a double reflected shock flowfield based on ICFC and named it ICFC+ (which stands for internal conical flow "C+"), which can effectively reduce the length of inlet and has a better starting ability in low Mach numbers. Ding et al. [28] integrated the basic flowfield of the waverider and waverider inlet. The generated airplane can ride on the shock at both the forebody and afterbody. Zhang et al. [29] developed an inward-turning waverider forebody/inlet basic flowfield that can eliminate the lip shock wave at the shoulder point. Considering that the total aerodynamic force performance is the main concern for gliding vehicles, the waverider inlet basic flowfield should be reasonably modified in the application.

The spatial arrangement of the flowfield slices also has an important influence on the volume performance of the waverider. Under the osculating framework, it is mainly determined by the flow capture curve (FCC), the inlet capture curve (ICC), etc. Chen et al. [6] developed a volume-improved osculating cone waverider using the variable curve of the curvature center of the ICC, which can improve the volumetric efficiency with little loss of performance compared with the conventional waverider. Following the vortex lift waveriders of Rodi [30], Wang et al. [11], Lobbia and Suzuki [31], and Liu et al. [32] studied the geometrical relationship among the FCC, the ICC, and the planform contour; and they proposed the double-sweep waveriders where the shock effect and vortex effect are employed to improve the hypersonic and subsonic performances, respectively. In this class of vortex lift waveriders, the low-speed-friendly planform contour leads to a thinner outward part and the centerbody provides the main loading space. Zhao et al. [9] developed another class of vortex lift waveriders where the planform contour has constant sweep angle. The designed cuspidal waverider has a significant nonlinear vortex-generated lift and better high-speed performance than the osculating waverider with the same volumetric efficiency. Zheng et al. [33] developed the multiple osculating cones' waverider design method for the ruled shock surface, which removes the constraint of imposing a specific conical flowfield to all osculating planes and offers another approach to improve the volume performance of waverider. Similar studies can be found in Refs. [34,35]. In the design process of the cone-derived method, the thickness of the waverider in each osculating plane is directly determined by the intersection position of the osculating plane and the FCC. However, in the conventional cone-derived method, the FCC is limited to have only one intersection point with the osculating plane to curb the transverse flow and keep the waverider characteristic. This limitation leads to a fast decrement of the thickness in the spanwise direction. If this limitation is broken at the cost of small aerodynamic performance loss, the volume of cone-derived waveriders can be significantly improved.

In this study, a novel design method is developed to improve the volume performance of large-slenderness-ratio cone-derived waveriders. Under the idea mentioned earlier in this paper of improving volume performance, an M-shaped FCC and an improved basic flowfield are developed. The designed FCC breaks the limitation that the FCC has only one point of intersection with the osculating plane and lifts the position of the most points of intersection. The improved basic flowfield extends the compression zone of the conventional basic flowfield and adds an additional reflected shock. Then, two groups of large-slenderness-ratio waveriders are designed by the novel method and the conventional cone-derived method, respectively. To better investigate the volume performance of large-slenderness-ratio waveriders and guide the design of volume-improved waveriders, an improved evaluation

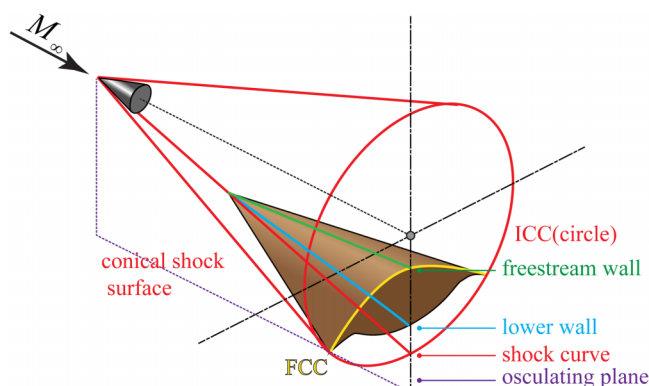


Fig. 1 Schematic of cone-derived waverider.

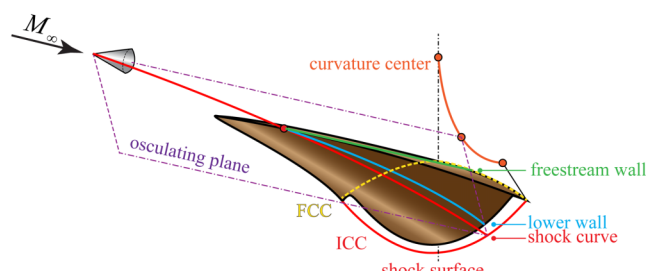


Fig. 2 Schematic of osculating cone waverider.

method is developed. In the developed evaluation method, a concept of an envelope box is introduced to represent the occupied space, a statistical method is developed to quantitatively describe the inner space that can be used to set loads, and a simulation method of the upper wall expansion is introduced to quantitatively describe the upper wall expansion performance. Then, the volume performances of the waveriders are studied in detail by the developed evaluation method. Finally, the aerodynamic performance of the volume-improved waverider is analyzed and compared with the conventional waveriders by numerical simulation under various freestream conditions.

II. Design Method of the Volume-Improved Cone-Derived Waverider

The design method proposed in this study consists of the design of the basic flowfield and the generation of the waverider. For convenience of discussion, the conventional cone-derived waverider and the volume-improved cone-derived waverider are named the CDW and VCDW, respectively.

A. Principle of the Design Method

The main inner space of the waverider is located in the aft section, which corresponds to the compression zone of the basic flowfield. Hence, the volume performance and loading capacity of the waverider can be effectively improved by extending the compression zone of the conventional basic flowfield. The basic flowfield of the VCDW is correspondingly designed, as shown in Fig. 3. An additional reflected shock and its dependent zone are also included because the high-pressure flow behind the reflected shock can be used to perform active flow control for the tailless aerodynamic configuration in the future. The numerical approach employed in the current study to design the basic flowfield is the method of characteristics (MOC) [36], which can inversely design the wall contour according to the wall pressure distribution. The control equations of the MOC are Eqs. (1) and (2). Along the streamline,

$$\begin{cases} \rho V dV + dp = 0 \\ dp - a^2 d\rho = 0 \\ \left(\frac{dy}{dx}\right)_0 = \tan(\theta) \end{cases} \quad (1)$$

Along the Mach line,

$$\begin{cases} \frac{\sqrt{Ma^2 - 1}}{\rho V^2} dp_{\pm} \pm d\theta_{\pm} + \frac{\sin \theta dx_{\pm}}{y Ma \cos(\theta \pm \alpha)} = 0 \\ \left(\frac{dy}{dx} \right)_{\pm} = \tan(\theta \pm \alpha) \\ \theta = \arctan(v/u) \\ \alpha = \arctan(1/Ma) \end{cases} \quad (2)$$

where V , a , p , u , v , Ma , x , y , and θ are the velocity magnitude, speed of sound, static pressure, horizontal velocity component, vertical velocity component, Mach number, horizontal coordinate, vertical coordinate, and flow angle, respectively. Furthermore, “+” represents the left-running Mach line and “-” means the right-running Mach line.

Figure 4 illustrates the characteristic grid of the basic flowfield of the VCDW, which consists of three zones: leading-edge shock-dependent zone, compression zone, and reflected shock-dependent zone. Because the MOC is an inviscid calculation method, walls ABC and DE can be represented as streamlines. The leading-edge shock-dependent zone is constructed from starting triangle cell 1, and its size is determined by the dimensionless size R . Points X1 and X2 of cell 1 have the same flow parameters, which are calculated by the oblique shock relation and the compression angle δ . In addition, the distance between points X1 and X2 should be small to reduce error. Then, the characteristic grid of the leading-edge shock-dependent zone is built by using cell 2, cell 3, and cell 4, which consist of the shock, left-running Mach line, right-running Mach line, and streamline. To improve the precision of the solution, some points can be added to the right Mach line of cell 4: the flow parameters of which are obtained by linear interpolation. Based on boundary Mach line BD of the first zone, the compression zone is similarly constructed with cell 5 and cell 6. The construction of the reflected shock starts from point D in the compression zone and consists of the predictor step and corrector step. Here, shock segment DX34 is used as an example to introduce the construction of each segment of the reflected shock. In the predictor step, the initial slope k_{D34} of shock segment DX34 is calculated by $\tan(\beta_D)$ with the shock relation [37]

$$\tan \theta_r = 2 \cot \beta_r \frac{Ma_0^2 \sin^2 \beta_r - 1}{Ma_0^2(\gamma + \cos 2\beta_r) + 2} \quad (3)$$

where θ_r , β_r , and Ma_0 are the relative flow angle, relative shock angle, and before-shock Mach number in the local coordinate system, respectively. The X axis of the local coordinate system is parallel to the before-shock flow velocity vector V_0 . The relative flow angle θ_r is the angle between V_0 and the aftershock flow velocity vector V_1 . This paper assigns θ_r of every point on the reflected shock to be $\theta_r = -\theta_D/2$. Here, θ_D is the before-shock flow angle at point D, and its value can be obtained from cell 4 in the process of constructing the leading-edge shock-dependent zone, as shown in Fig. 4. Point X34 is the intersection of shock segment DX34 and Mach line X3X4, and its flow parameters can be evaluated by linear interpolation [Eq. (4)]:

$$\left\{ \begin{array}{l} \Lambda_{X34} = \xi \Lambda_{X3} + (1-\xi) \Lambda_{X4} \\ \Lambda = \theta, \rho, p, V \\ \xi = \frac{x_{34} - x_4}{x_3 - x_4} \text{ or } \frac{y_{34} - y_4}{y_3 - y_4} \end{array} \right. \quad (4)$$

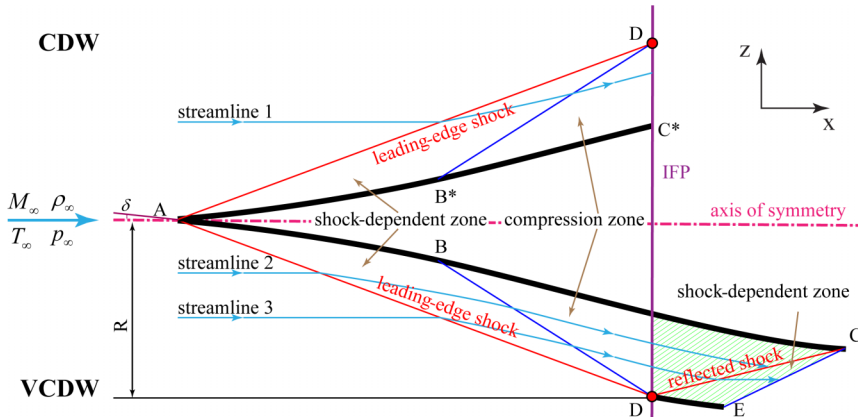


Fig. 3 Basic flowfield of VCDW (lower one) and CDW (upper one). (Note that IFP represents plane where ICC and FCC are located.)

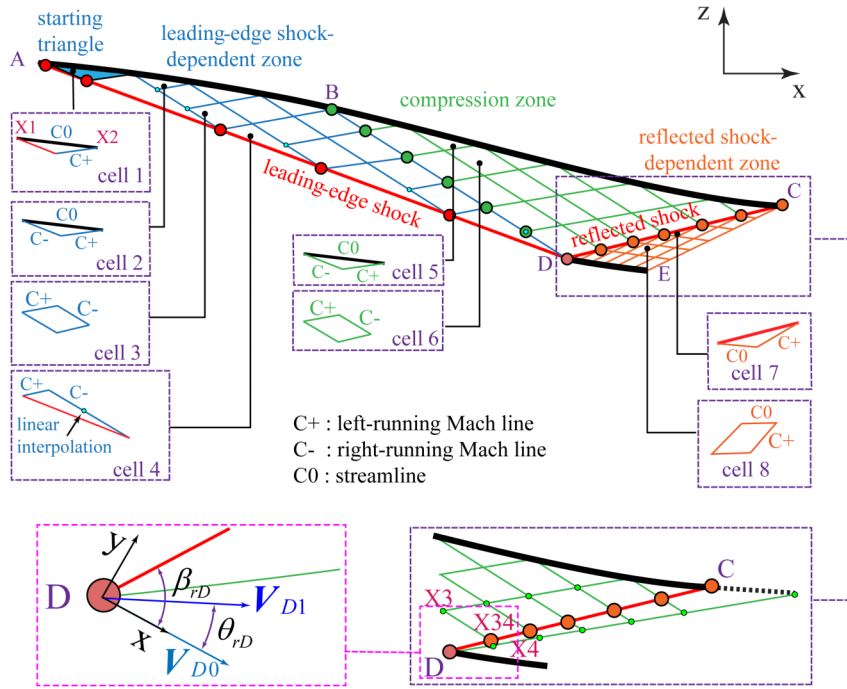


Fig. 4 Characteristic grid of basic flowfield of VCDW.

The predictor step is finished after evaluating the shock angle of point X34 by Eq. (3). In the corrector step, the slope of shock segment DX34 is corrected as

$$\kappa_{DX34} = (\beta_D + \beta_{X34})/2 \quad (5)$$

Then, the position of point X34 is recalculated by line DX34 with this new slope and Mach line X3X4. The parameters of point X34 are also evaluated by Eq. (4), and the slope of shock segment DX34 is corrected by Eq. (5). The final shock segment can be obtained by repeating the corrector step until the change of flow parameters at point X34 are less than a specified tolerance. The construction of the rest of the reflected shock is also similar. After discarding the aftershock part of the compression zone, the reflected shock-dependent zone is constructed with cell 7 and cell 8 based on the aftershock flow parameters of each point on the reflected shock.

Based on the designed basic flowfield, the volume-improved waverider can be generated from the designed FCC and ICC. In the cone-derived method, the ICC is a circle. Considering that the upper wall expansion performance needs a flat FCC on the top and the space utilization and loading capacity need a FCC with a regular shape, an M-shaped FCC is designed, as shown in Fig. 5. Curve AB corresponds to the main body of the VCDW and has only one point of intersection (e.g., i1) with the osculating plane (e.g., OP 1). Curve BFD corresponds to the sidewall of the VCDW and has two points of intersection (e.g., i21 and i22) with the osculating plane (OP; e.g., OP 2). Curve AD corresponds to the CDW and has only one point of intersection (e.g., i3) with the osculating plane (e.g., OP 1). The designed M-shaped FCC of the VCDW can significantly lift the intersection position of the FCC and most osculating planes, which finally leads to a volume increment of the VCDW. The leading edge can be obtained by projecting the FCC along the freestream direction onto the shock surface of the conical flowfield. The lower wall of the waverider can be obtained by tracing streamlines from each point of the leading edge in the conical flowfield. Streamline 2 is selected to generate the lower wall of the main body, and streamline 3 is chosen to generate the sidewall, as shown in Figs. 3 and 5. Streamline 2 stops at curve CD to avoid the shock drag caused by the reflected shock. Streamline 3 stops at curve CE, and its segment in the reflected shock-dependent zone is prepared for aerodynamic control in the future. The upper surface of the waverider simply uses the freestream surface. The schematic of the VCDW is shown in Fig. 6.

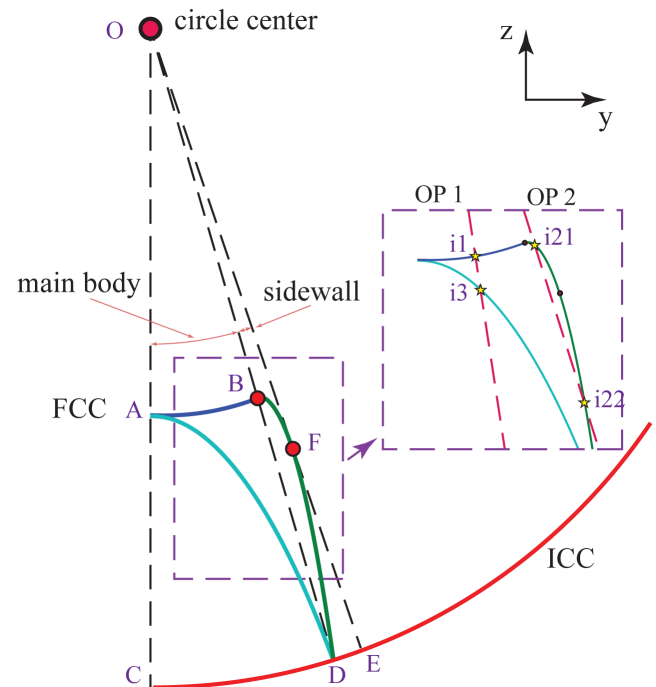


Fig. 5 Comparison of FCC between VCDW (curve ABFD) and CDW (curve AD).

B. Validation of the Design Method

In the proposed design method, the design of the basic flowfield is based on the MOC and the generation of the waverider is based on the cone-derived method. Considering that the validation of the waverider generation method needs the three-dimensional flowfield information, this part of the work is placed in Sec. IV.B. The basic flowfield is designed by the MOC with the parameters listed in Table 1. Then, the results obtained by the MOC are compared with the inviscid numerical results simulated by computational fluid dynamics (CFD) to validate the design method. ANSYS Fluent (with the second-order AUSM scheme and Green-Gauss gradient method) is used as the numerical tool for CFD simulation. The computational

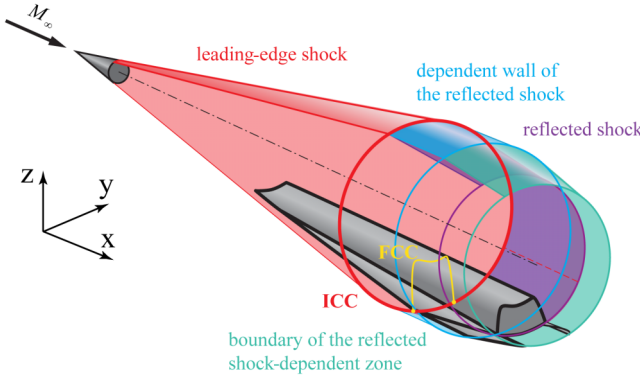


Fig. 6 Schematic of VCDW.

Table 1 Design parameters of the basic flowfield

Parameter	Value
H, km	40
M_∞	12
p_∞ , Pa	287.14
ρ_∞ , kg/m ³	0.004
T_∞ , K	250.35
R^c	900
α , ° ^a	0
δ , ° ^b	1
Wall pressure law ^d	$p = p_0(1 + 0.0002x)$

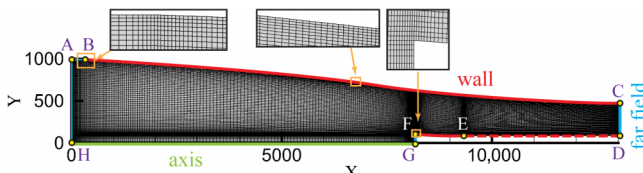
^a α is the angle of attack of the freestream.^b δ is the leading-edge compression angle.^c R is the dimensionless size, as shown in Fig. 3.^dIn the wall pressure law, p_0 is the aftershock static pressure at the leading edge and x is the horizontal distance starting from the leading edge.

Fig. 7 Computational grid for the designed basic flowfield (in units of millimeters).

grid with 24,146 cells is used, as shown in Fig. 7. Curves BC and FE are the designed wall of the basic flowfield. Figure 8 shows the pressure contour simulated by the MOC and CFD. Clearly, the structures of the flowfields simulated by the MOC and CFD are highly similar. The end positions of the two reflected shocks are almost coincident. In addition, no significant difference is found in the pressure distribution of the lower and upper walls between the results of the MOC and CFD, as shown in Fig. 9. It is remarkable that

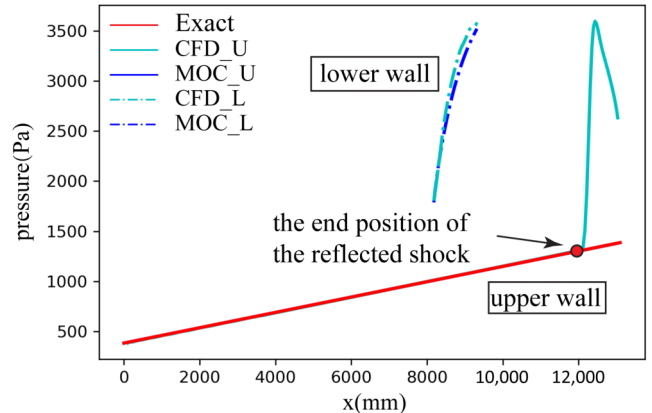


Fig. 9 Pressure distribution of lower wall and upper wall simulated by MOC and CFD. (Note that “_U” represents the upper wall and “_L” represents the lower wall.)

the pressure distribution of the designed upper wall perfectly meets the design requirement, which is labeled as “Exact.” All the results mentioned earlier in this paper validate the design method of the basic flowfield.

C. Generation of the Waveriders

Figure 10 shows the models of the VCDW, CDW, and three additional comparable waveriders (CWs) named CW1-1, CW1-2, and CW2-1. Because their basic flowfields have the same design parameters (as shown in Table 1) but different shock structures, the five waveriders can be regarded to be designed from the same basic flowfield but with different types of streamlines. Here, CW1-1 and CW2-1 use streamline 1; CW1-2 and CDW choose streamline 2; and the main body and sidewall of the VCDW select streamline 2 and streamline 3, respectively. The expressions and parameters of the FCC and ICC are listed in Table 2, which are selected for a large slenderness ratio. Here, the FCC of the VCDW, CW1-1, and CW1-2 are curve ABFD; and that of the CW2-1 and CDW are curve AD. The slenderness ratio of the VCDW is 9.604 (with sidewall) or 8.718 (without sidewall), whereas the slenderness ratio of the CDW is 9.23. All the essential geometrical parameters of the five waveriders are shown in Table 3.

III. Improved Evaluation Method for Volume Performance

The improved evaluation method developed in this study consists of the evaluation of space utilization, loading capacity, and upper wall expansion performance. For conciseness of the developed evaluation method, the inner structural arrangement of the waverider is ignored.

A. Evaluation of the Space Utilization

As mentioned in Sec. I, the most widely used volumetric efficiency can be expressed as Eq. (6) (Ref. [5]) and Eq. (7) (Ref. [6]), where V_w , $S_{w\text{-wet}}$, and $S_{w\text{-p}}$ are the volume, wetted area, and projected area of the waverider, respectively. However, these two equations are inadequate

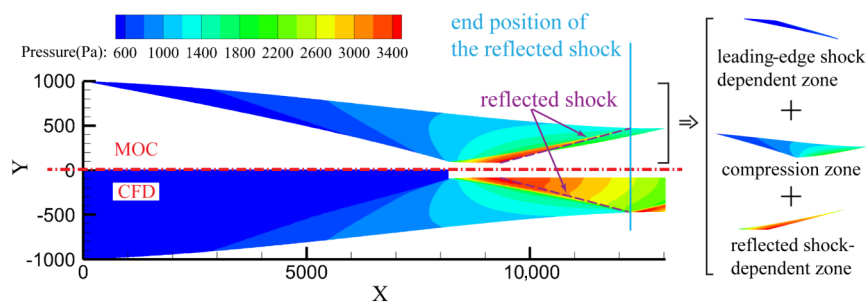
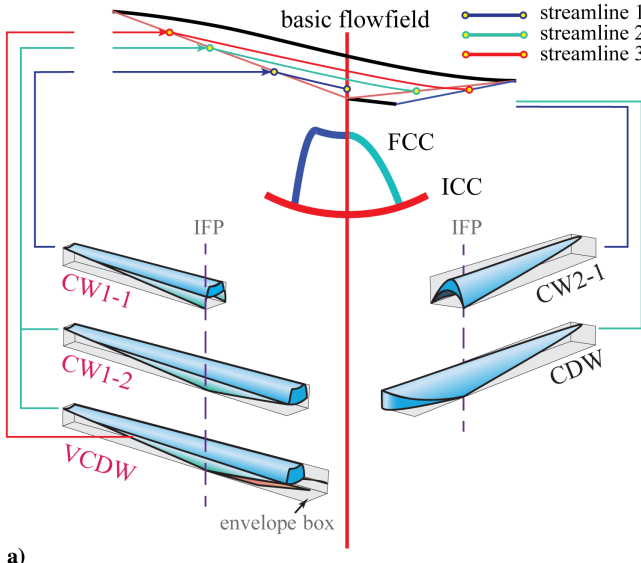


Fig. 8 Pressure contour simulated by the MOC (the upper one) and CFD (the lower one) (in units of millimeters).



a)

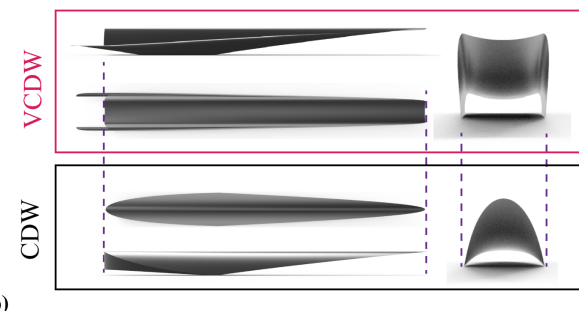


Fig. 10 Designed waveriders: a) relations between the waveriders and the basic flowfield, and b) three views of VCDW and CDW.

Table 2 Expressions of the FCC and the ICC (in units of millimeters)

Curve	Function	<i>a</i>	<i>b</i>	<i>c</i>
FCC				
AB	$y^2 + z^2 = a^2$	2200	—	—
BFD	$z = ay^2 + by + c$	-0.0065	8.856	-5124.95
AD	$z = ay^2 + b$	-0.0011	-2200	—
ICC				
CDE/CD	$y^2 + z^2 = a^2$	4000	—	—

Table 3 Geometrical parameters of the five waveriders

Name	<i>L</i> , m	<i>W</i> , m	<i>H</i> , m	$S_{w-\text{wet}}/\text{m}^2$	S_{w-p}/m^2	V_w/m^3
CW1-1	14.436	2.400	1.721	69.65	29.127	9.175
CW1-2	22.153	2.541	1.769	118.746	48.257	24.024
VCDW	24.403	2.541	1.769	121.44	49.386	24.024
CW2-1	14.436	2.400	1.616	59.913	22.137	6.007
CDW	22.153	2.400	1.616	104.174	36.376	16.267

to evaluate the utilization of the occupied space in the case of a large-slenderness-ratio waverider. One of the most important factors is the reasonability of the expression of the occupied space.

$$\eta_{\text{wet}} = V_w^{2/3} / S_{w-\text{wet}} \quad (6)$$

$$\eta_p = V_w^{2/3} / S_{w-p} \quad (7)$$

To better evaluate the space utilization, the concept of the envelope box (A1B1C1D1-A2B2C2D2) is introduced to represent the space

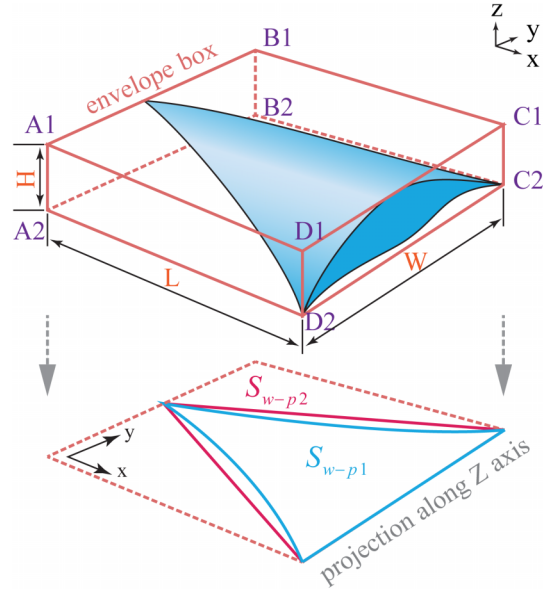


Fig. 11 Illustration of the envelope box.

occupied by the waverider, as shown in Fig. 11. The envelope box is the smallest cuboid that can envelop the waverider, and its six surfaces are parallel to the corresponding coordinate plane. In this case, the envelope box has the same length and width as the waverider. For practical application, the envelope box can be replaced by the corresponding shape, which is determined in advance by the design task (e.g., a taperlike fairing) and is irrelevant to the size of the designed waverider. The different projected area (e.g., S_{w-p_2} and S_{w-p_1}) may lead to a same occupied area, as shown in Fig. 11. Based on the concept of the envelope box, two variables are developed to evaluate the utilization rate and efficiency of the occupied space, including volumetric efficiency $\eta_{\text{eb}-p}$ [Eq. (8)] and the standard volume ratio $\text{VRT}_{w/\text{eb}}$ [Eq. (9)]. Here, V_{eb} , $S_{\text{eb}-p}$, L , and W are the volume, Z-axis projected area, length, and width of the envelope box, respectively:

$$\eta_{\text{eb}-p} = V_w^{2/3} / S_{\text{eb}-p} = V_w^{2/3} / (LW) \quad (8)$$

$$\text{VRT}_{w/\text{eb}} = V_w / V_{\text{eb}} = V_w / (LWH) \quad (9)$$

The results in Fig. 12 show the space utilization evaluated by different evaluation variables. In the conventional evaluation method, η_{wet} shows that VCDW and CW1-2 both perform better than CDW, whereas η_p draws a conflicting conclusion. However, the VCDW has 48% larger volume and only 16% more occupied area than the CDW. In the new evaluation method, $\eta_{\text{eb}-p}$ and $\text{VRT}_{w/\text{eb}}$ show that the VCDW, CW1-1, and CW1-2 have obvious better evaluation results than the corresponding conventional waveriders, as shown in Fig. 12b. Therefore, the new evaluation method can obtain a better result in evaluating the space utilization of large-slenderness-ratio waveriders. In addition, the developed method also reveals the advantage of the designed M-shaped FCC in space utilization.

B. Evaluation of the Loading Capacity

The special cross-sectional shape of the waverider determines that only part of the inner space can be used to set loads, which limits the application of the volumetric efficiency in evaluating the loading capacity. To better evaluate the loading capacity, a statistical method named the load test is developed, which consists of two-dimensional (2-D) and three-dimensional (3-D) sampling, as shown in Fig. 13.

In the process of 2-D sampling, a series of rectangles that represent loads is constructed to test the loading capacity of the cross section of the waverider, as shown in Figs. 13a and 13b. The rectangle is named load2D and its quantity is named the 2-D sampling number. Load2D is built from the starting line (line A1D and EH1), which locates in the

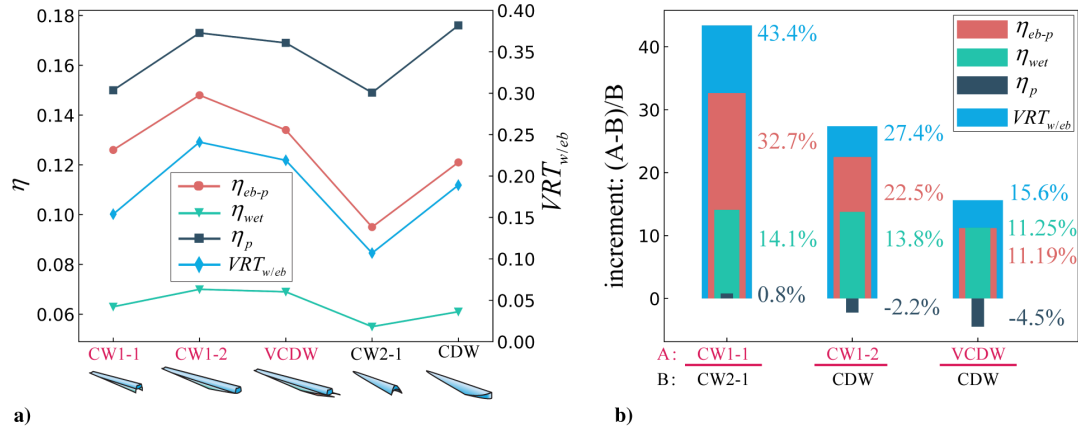


Fig. 12 Evaluation of the space utilization: a) volumetric efficiency and volume ratio of the waveriders, and b) comparison of volumetric efficiency and volume ratio between each pair of waveriders.

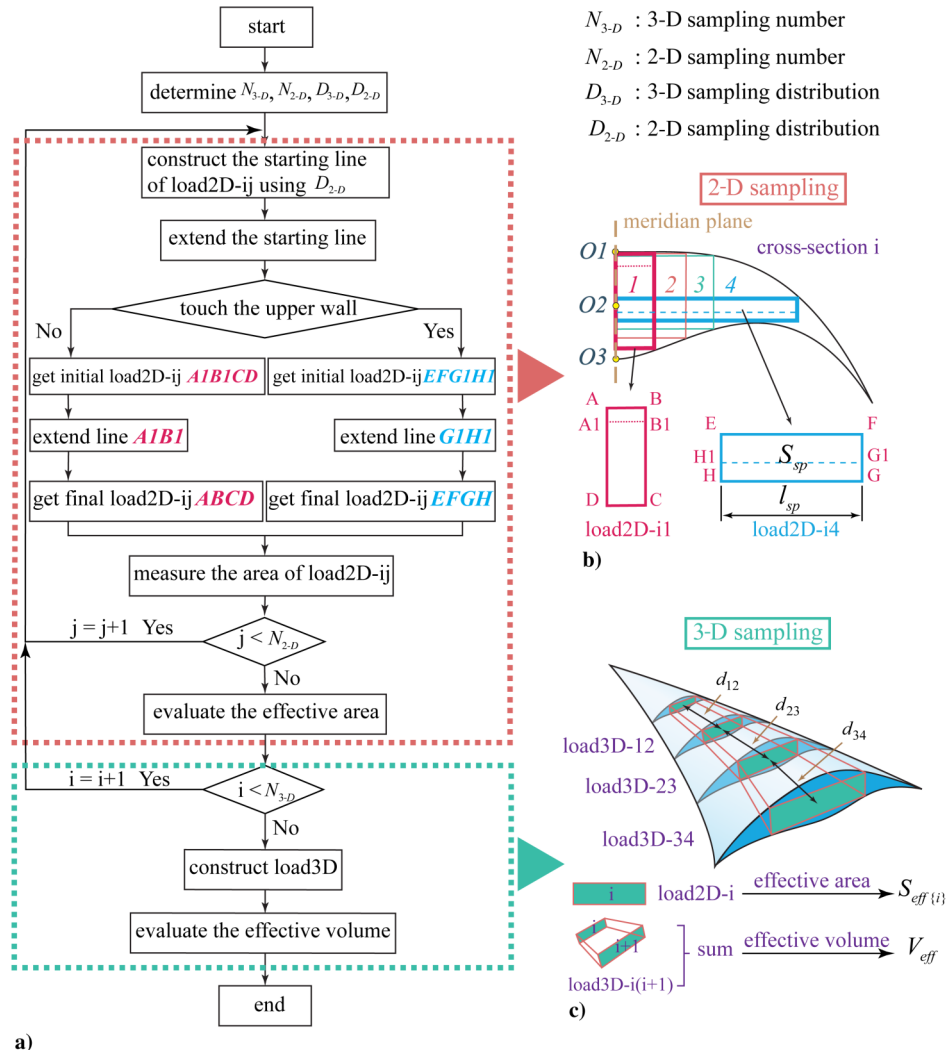


Fig. 13 Illustration of the load test (both 2-D and 3-D sampling numbers are four): a) flowchart of load test, b) illustration of 2-D sampling, and c) illustration of 3-D sampling.

meridian plane and has the same midpoint (O_2) as line O_1O_3 . The length ratio of each starting line to line O_1O_3 is named the 2-D sampling distribution. Then, the initial load2D (rectangle $AIB1CD$ or $EFG1H1$) can be obtained by extruding the starting line (line $A1D$ or $E1H$) until touching the upper wall or lower wall. The final load2D (rectangle $ABCD$ or $EFGH$) is constructed by extruding the corresponding edge (line $A1B1$ or $H1G1$) of the initial load2D (rectangle

$A1B1CD$ or $EFG1H1$) until touching another wall. Finally, the equivalent area of the cross section that can be used to set loads is evaluated by Eq. (5) and named the effective area. The effective area has considered the influence of the contour shape of each cross section. Here, l_{sp} is the length of load2D and $S_{sp}(l)$ is the polynomial fitting curve of the load2D area to the load2D length, as shown in Fig. 13b:

$$S_{\text{eff}\{i\}} = \int_{\min(l_{sp})}^{\max(l_{sp})} S_{sp}(l) dl / (\max(l_{sp}) - \min(l_{sp})) \quad (10)$$

In the process of 3-D sampling, a series of cross sections is selected to perform 2-D sampling, and their quantity and positions are named the 3-D sampling number and 3-D sampling distribution, respectively, as shown in Figs. 13a and 13c. The 3-D sampling distribution can either be uniform or coincide with the specific positions determined by the design task. In each cross section, a virtual rectangle is built after finishing 2-D sampling and its area equals the effective area. Then, virtual hexahedrons named load3D are constructed by connecting an adjacent pair of virtual rectangles. Finally, the sum of the volume of each load3D is used to evaluate the volume of wavewider, which can be used to set loads and named effective volume, as shown in Eq. (11). Here, $d_{i(i+1)}$ is the distance between the i th and $i + 1$ th cross section, and $n_{sp(3D)}$ is the 3-D sampling number. Based on effective volume, the volume ratio $\text{VRT}_{\text{eff}/w}$ [defined as Eq. (12)] and volume ratio $\text{VRT}_{\text{eff}/eb}$ [defined as Eq. (13)] are introduced to evaluate the loading capacity:

$$V_{\text{eff}} = \sum_{i=1}^{n_{sp(3D)}-1} (S_{\text{eff}\{i\}} + S_{\text{eff}\{i+1\}}) \times d_{i(i+1)} / 2 \quad (11)$$

$$\text{VRT}_{\text{eff}/w} = V_{\text{eff}} / V_w \quad (12)$$

$$\text{VRT}_{\text{eff}/eb} = V_{\text{eff}} / V_{eb} \quad (13)$$

To determine the 2-D sampling number and 2-D sampling distribution of the VCDW and CDW for the following work, six 2-D sampling distributions are designed in the plane where the ICC and FCC are located, as shown in Table 4. It is natural that a larger 2-D sampling number leads to a more exact 2-D sampling results, and the main effort is therefore focused on the influence of the 2-D sampling distribution. Figures 14a and 14b describe the sampling results and their third-order polynomial fitting curves. A uniform 2-D sampling distribution leads to a serious nonuniform distribution of sampling points, which generates a wrong fitting curve for the VCDW. Consequently, the nonuniform 2-D sampling distributions are selected that can balance the quantity of the sampling points on both sides of the entire sample results. Figures 14c and 14d reflect the influence of

Table 4 2-D sampling distributions^a

Name	1	2	3	4	5	6	7	8	9	10
4U	0.2	0.4	0.6	0.8	1.0	—	—	—	—	—
6U	0.143	0.286	0.429	0.571	0.714	0.857	1.0	—	—	—
9U	0.1	0.2	0.3	0.4	0.5	0.6	0.7	0.8	0.9	1.0
4NU	0.1	0.2	0.95	0.98	1.0	—	—	—	—	—
6NU	0.1	0.2	0.50	0.80	0.95	0.98	1.0	—	—	—
9NU	0.1	0.2	0.40	0.50	0.60	0.70	0.80	0.95	0.98	1.0

^a4U and 4NU, respectively represent uniform and nonuniform distribution with a 2-D sampling number equaling four; others are similar. The value of 1.0 is not counted in the 2-D sampling number because the area of load2D will always be zero when the starting line coincides with line OIO3.

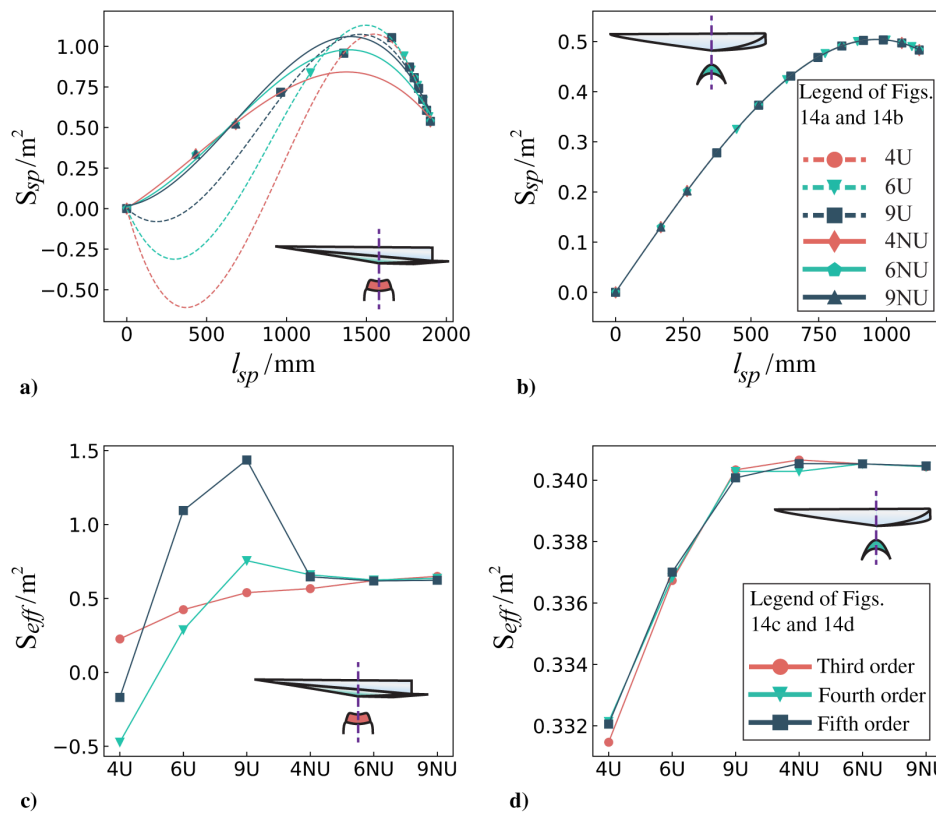


Fig. 14 Influence of the sampling distributions a), b) and the fitting curve order c), d) on the sampling results.

the order of the polynomial fitting curve. Increasing the order of the fitting curve is an efficient approach to improve the precision, whereas it cannot repair the wrong fitting curves of the uniform 2-D sampling distributions. Compared with the other five distributions in Table 4,

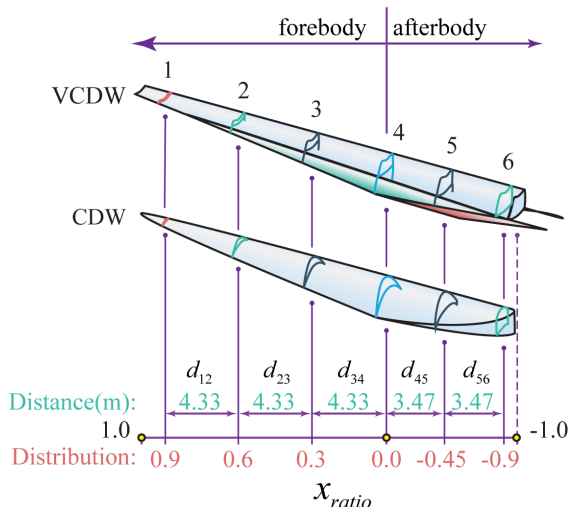


Fig. 15 3-D sampling distributions of VCDW and CDW.

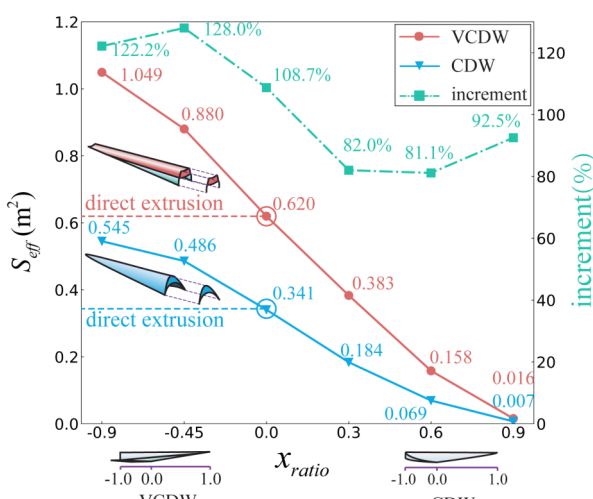


Fig. 16 Effective area of VCDW and CDW.

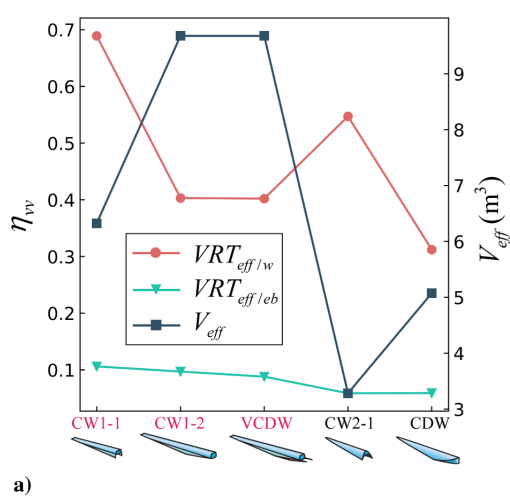


Fig. 17 Evaluation of loading capacity: a) volume ratio and effective volume of waveriders, and b) volume ratio and effective volume comparison among three sets of waveriders.

the 2-D sampling distribution 6NU with the third-order polynomial fitting curve is adopted because it has enough accuracy and relatively low operational complexity. For simplicity, a uniform 3-D sampling distribution is adopted, as shown in Fig. 15.

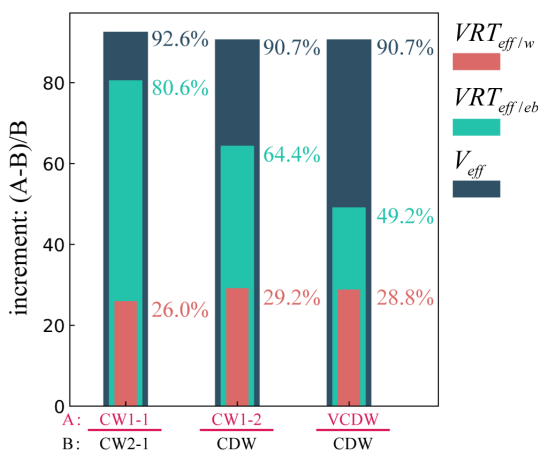
The results of Fig. 16 show that the effective area of each cross section of the VCDW is nearly two times larger than that of the CDW and has an obvious advantage in the afterbody. Hence, the M-shaped FCC can significantly improve the effective area and can obtain more benefits from the developed basic flowfield. In addition, the effective area increases with the distance measured from the nose of waverider. Therefore, by comparing with the direct extrusion of the cross-sectional contour in the plane where the ICC and FCC are located, the improved basic flowfield can effectively increase the effective area of the cross sections in the afterbody.

The results in Fig. 17 reflect the advantage of the VCDW in the effective volume, including about a 90% larger effective volume, a 50% larger volume ratio $VRT_{eff/eb}$, and a 30% larger volume ratio $VRT_{eff/w}$ than the CDW. Furthermore, CW1-2 and the CDW have larger volume ratios than CW1-1 and CW2-1, respectively, which reflects that the developed basic flowfield can significantly improve the performance of the loading capacity, as shown in Fig. 17a. CW1-1 and CW1-2 perform better in volume ratio than CW2-1 and the CDW, respectively, as shown in Fig. 17b, which proves the advantage of the designed M-shaped FCC in loading capacity. In conclusion, the novel design method can effectively improve the loading capacity of the large-slenderness-ratio waverider.

C. Evaluation of the Upper Wall Expansion Performance

The initial upper wall surface of the waverider generally needs to be expanded to increase the volume. In the upper wall expansion, the volume growth rate directly influences the final choice of waverider and the area growth rate of each cross section affects the method of the upper wall expansion. Hence, the upper wall expansion performance can be represented by the volume growth rate and area growth rate. In this section, a simulation method of the upper wall expansion is developed to quantitatively evaluate the upper wall expansion performance.

In the developed simulation method, a specific number (named the expansion number) of expansion simulations are performed in each cross section, as shown in Fig. 18. The selection method of the cross section is same as that of Sec. III.B, and therefore described by the 3-D sampling number and 3-D sampling distribution. In the i th cross section and the j th expansion process of the simulation method, the midpoint A_j of the upper wall is obtained by moving initial midpoint A_1 over a distance (named the expansion distance) of $\delta = j\Delta h$. Two lines starting from A_j and tangent to the initial upper wall are chosen to represent the upper wall after expansion. For a general cross-sectional contour, this operation can be conveniently carried out in the CAD software. If there is no tangent point, the two lines are



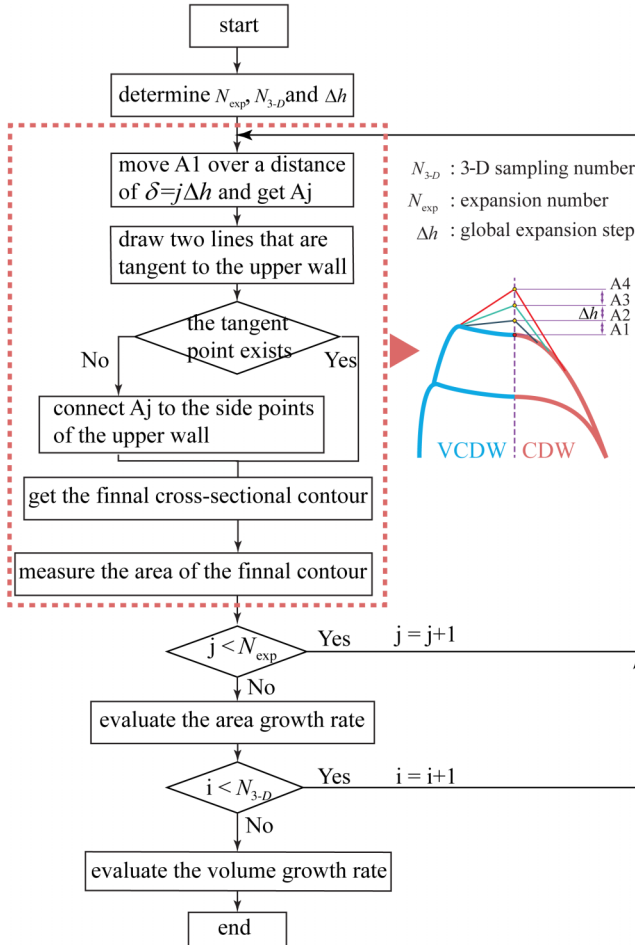


Fig. 18 Flowchart of the simulation method of the upper wall expansion.

constructed by connecting the side points of the initial upper wall with A_j . The new cross-sectional contour is a merger between the initial cross-sectional contour and the two lines. The area of the new and initial cross sections are represented as $S_{i(j)}$ and $S_{i(0)}$, respectively. Then, the area growth rate can be evaluated by Eq. (14), which is defined as the first-order derivative of the polynomial fitting curve $f_i(\delta) = (S_i(\delta) - S_{i(0)})/S_{i(0)}$ at position $\delta = 0$. Here, $S_i(\delta)$ is the area of the expanded cross-sectional contour with the expansion distance equals δ . The effective area and area growth rate of each cross section can offer an initial reference for the load placement about whether the space between each pair of cross sections is enough

for a specific load and whether the space shortage can be solved by local upper wall expansion:

$$G_{\text{exp and}}^{Si} = \frac{d((S_i(\delta) - S_{i(0)})/S_{i(0)})}{d\delta} = \frac{dS_i(\delta)}{S_{i(0)} d\delta} \Big|_{\delta=0} \quad (14)$$

Similarly, the volume growth rate can be evaluated by Eq. (15), which is the first-order derivative of the polynomial fitting curve $F(\delta) = (V(\delta) - V_0)/V_0$ at position $\delta = 0$. Here, V_0 is the volume of the initial waverider and $V(\delta)$ is the volume of the expanded waverider with the expansion distance equal to δ :

$$\begin{cases} G_{\text{exp and}}^V = \frac{d((V(\delta) - V_0)/V_0)}{d\delta} = \frac{dV(\delta)}{V_0 d\delta} \Big|_{\delta=0} \\ V(\delta) = \sum_{i=1}^{n_{sp(3D)}-1} (S_i(\delta) + S_{i+1}(\delta)) \times d_{i(i+1)}/2 \end{cases} \quad (15)$$

In this study, the expansion number and Δh are assigned as 3 and 160 mm, which are nearly 10% of the height of the cross-sectional contour in the plane where the ICC and FCC are located. The results in Fig. 19 show that the VCDW is about 3.9 times larger than the CDW in the volume growth rate and has a significantly larger area growth rate in the selected cross sections. The area growth rate decreases as we go downstream from the head of the waverider ($x_{\text{ratio}} = 1.0$), which reflects that the head of the waverider can achieve a larger relative area increment under the upper wall expansion. At position $x_{\text{ratio}} = -0.45$, the area growth rate of the VCDW is about six times larger than the CDW. At position $x_{\text{ratio}} = 0.9$, the area growth rate of the VCDW is still nearly 1.8 times larger than the CDW. In conclusion, the VCDW has a significant advantage in the upper wall expansion performance.

IV. Validation of the Aerodynamic Performance

A. Numerical Method and Grids

In this study, the hypersonic flowfields of the designed waveriders are simulated by commercial software ANSYS Fluent, which has been validated in past studies [6,9,19,38]. The implicit density-based solver with the second-order AUSM scheme is selected due to its relatively accurate resolution of shock. The Green-Gauss method is used to calculate the gradient of the conserved variables. Considering the compressibility of the gas under the hypersonic condition, the ideal gas model is chosen. In the viscous case, the Reynolds-averaged Navier-Stokes equations are used. Then, a reasonable turbulence model is fundamental to the correct simulation of the flowfield and wall parameter distribution. To choose an optimal turbulence model, the widely used $k-\omega$ shear-stress transport (SST), standard $k-\epsilon$ and Spalart-Allmaras (S-A) models are tested in the simulation of the hypersonic flow passing a circular cylinder [39]. The inflow condition

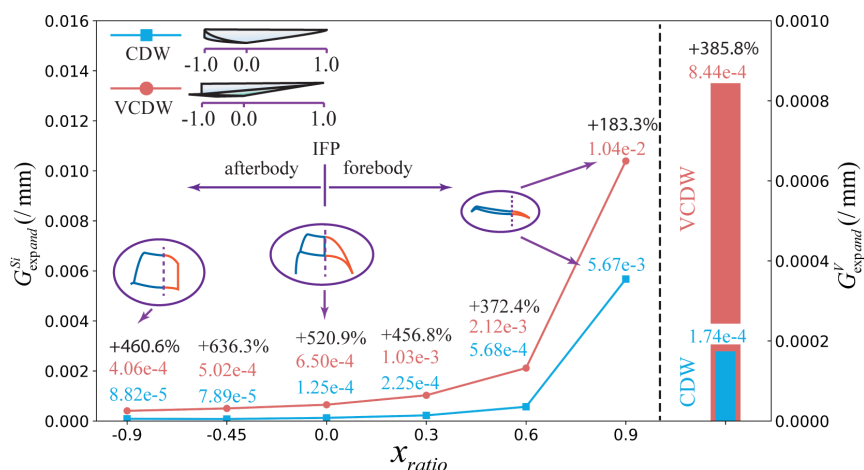


Fig. 19 Comparison of the volume growth rate and area growth rate between VCDW and CDW.

for the air is listed in Table 5, where M_∞ , T_∞ , and Re are the Mach number, static temperature, and Reynolds number of the inflow, respectively; and T_w is the static temperature of the wall. A computational grid with 100×100 cells is used, and the thickness of the grid cell closest to the wall is $1.0e - 5$, as shown in Fig. 20. Clearly, the wall pressure distribution obtained by the $k-\omega$ SST model is closest to the experimental data. Consequently, the $k-\omega$ SST turbulence model is selected in the following sections, which is also the choice of Refs. [5–8]. The

Table 5 Inflow condition for the air

Parameter	Value
M_∞	8.03
T_∞, K	124.94
T_w, K	294.44
Re	1.835×10^5

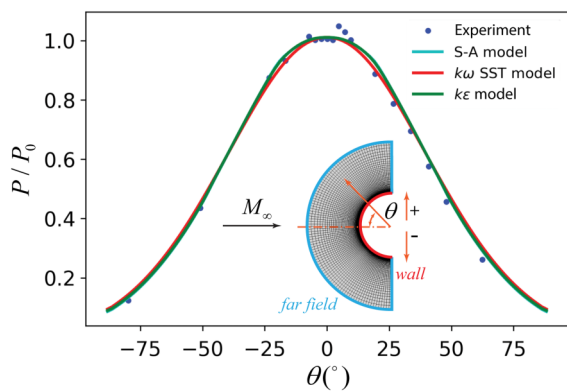


Fig. 20 Pressure distributions with different turbulence models.

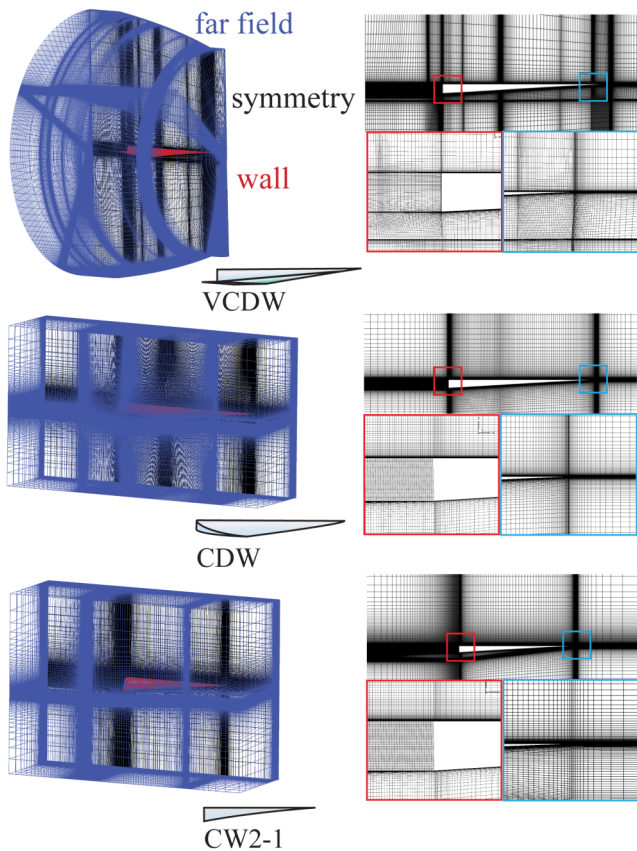


Fig. 21 Computational grids of VCDW, CDW, and CW2-1.

viscosity coefficient is calculated by the kinetic theory. The specific heat ratio γ is assigned as 1.4.

To validate the grid independence, three structured grids with different cell counts are generated for half the models of the VCDW, CDW, and CW2-1 on one side of the plane of symmetry, as shown in Fig. 21. The thickness of the grid cell closest to the wall for viscous cases is $1.0e - 5$ m, which ensures that $y+$ is less than five. The boundary-layer grid has 30 grid cells along the direction normal to the wall. In each grid, the wall is set as the no-slip and adiabatic wall boundary condition. The symmetry face is set as the symmetry boundary condition. The far field is set as the pressure far-field boundary condition. The solutions can be considered as converged when the residuals drop to $1.0e - 4$ and the values of lift and drag do not change at the four decimal places. The convergence history of the lift and drag of the CDW with the moderate grid at the design condition is given as an example, where the convergent result can be obtained after 10,184 iteration steps when the Courant–Friedrichs–Lowy number is set at 0.5, as shown in Fig. 22. The aerodynamic performance results of these grids at the design condition ($H = 40$ km and $Ma = 12$ in Table 6) are shown in Table 7. Here, $Cl = L/(q_\infty S_{w-p})$, $Cd = D/(q_\infty S_{w-p})$, L/D , and $q_\infty = \rho V^2/2$ are the lift coefficient, drag coefficient, lift-to-drag ratio, and freestream dynamic pressure, respectively. The projected area of the waverider is selected as the reference area for Cl and Cd . Considering the calculation cost and the precision of the result, the moderate grids are used for each waverider.

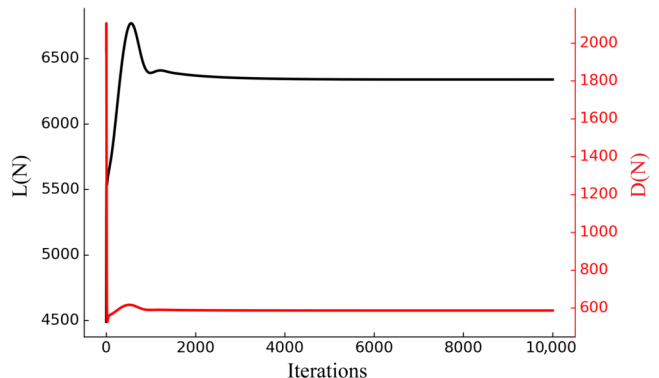


Fig. 22 Convergence history of lift and drag of CDW with the moderate grid at design condition.

Table 6 Freestream conditions at the various Mach numbers

H, km	Ma	p_∞, Pa	$\rho_\infty, \text{kg/m}^3$	T_∞, K
40 (design condition)	12	287.14	0.004	250.35
35	10	574.69	0.008	236.51
30	8	1197.03	0.018	226.51
25	6	2549.22	0.040	221.55

Table 7 Validation of grid independency

Model	Cases	Grid size	Cl	Cd	L/D
VCDW	Coarse	5,909,564	6.6671e-3	1.5394e-3	4.331
	Moderate	9,706,884	6.6690e-3	1.5407e-3	4.329
	Refined	12,554,874	6.6692e-3	1.5410e-3	4.328
CDW	Coarse	5,822,595	6.5997e-3	1.4091e-3	4.684
	Moderate	7,229,395	6.6008e-3	1.4098e-3	4.682
	Refined	9,143,265	6.6010e-3	1.4101e-3	4.681
CDW-1	Coarse	4,249,785	6.9488e-3	1.5779e-3	4.404
	Moderate	5,704,665	6.9492e-3	1.5787e-3	4.402
	Refined	8,129,465	6.9494e-3	1.5789e-3	4.401

B. Flowfields at Design Condition

The inviscid and viscous flowfields of the VCDW, CDW, and CW2-1 are analyzed numerically at the design condition ($H = 40$ km and $Ma = 12$ in Table 6). Since CW2-1 has the same geometrical shape and flowfield as the forebody of the CDW, its flowfield is not shown in this section.

Figure 23 shows the details of the inviscid flowfield of the VCDW. The head of the VCDW has no essential difference with the conventional cone-derived waverider. It can therefore ride on the shock, and no leakages of the high-pressure gas are found on both sides of waverider, as shown in Fig. 23a. Then, the existence of the sidewall leads to a unique double-shock structure which is composed of the weak upper shock and the strong lower shock, as shown in Fig. 23b. The upper shock is generated by the outward expansion of the sidewall, whereas the lower shock is generated by the main body. Because the sidewall expands outward, there is an expansion region near the “cowl lip” of the VCDW, which corresponds to part FD (as shown in Fig. 2) of the FCC, as shown in Fig. 23d. Then, the leading-edge shock is pulled inward by the expansion region and leads to the unique double-shock structure mentioned earlier in this paper. In the afterbody, the high-pressure gas generated by the reflected shock integrates with the compressed gas generated by the leading-edge shock and diffuses into the surrounding air, as shown in Figs. 23e, 23f, and 23c.

The comparison between the inviscid and viscous flowfields is shown in Fig. 24. Compared with the VCDW, the inviscid flowfield of the CDW is relatively simple. The forebody of the CDW rides on the shock, and the leakage of the high-pressure gas is only found in the afterbody. The details of the pressure contour from the front and side views of the selected cross sections are shown in Fig. 25. In position $x = 0$ of the CDW, the shape and location of the shock under the inviscid condition are in accordance with the designed results (displayed as a red dashed line). The results mentioned earlier in this paper validate the conventional cone-derived method, which is the foundation of the proposed novel waverider generation method. Due to the existence of the expansion region introduced by the sidewall of the VCDW, the shock position in the inviscid case is higher than the design position. This result is within our expectation because the design method breaks the limitation that the FCC has only one point of intersection with the osculating plane. Because there is no leakage of the high-pressure gas, the VCDW still rides on the shock and its

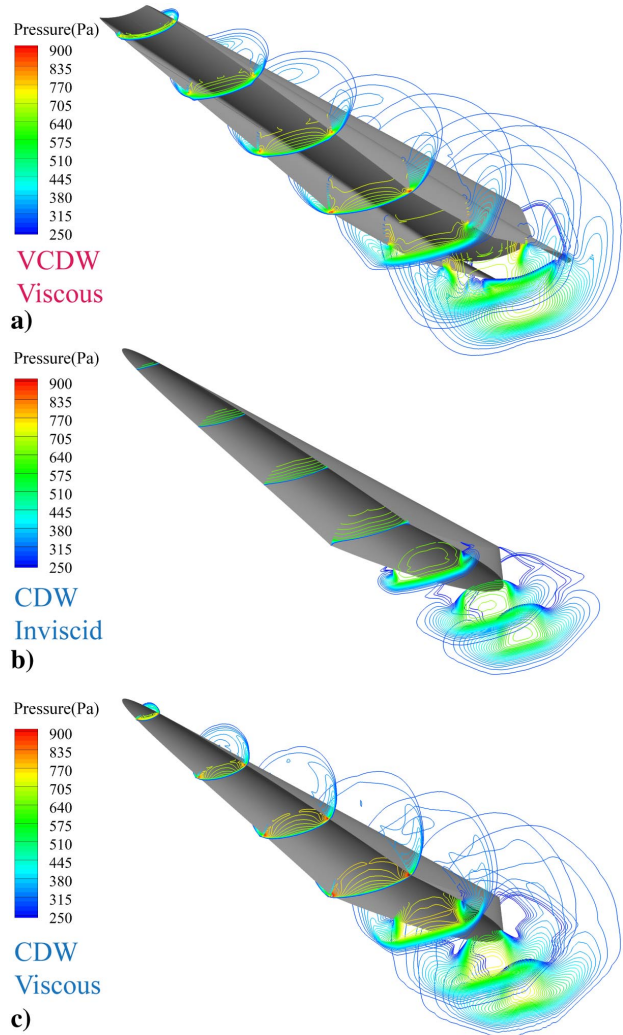


Fig. 24 Pressure contours of VCDW and CDW at design condition.

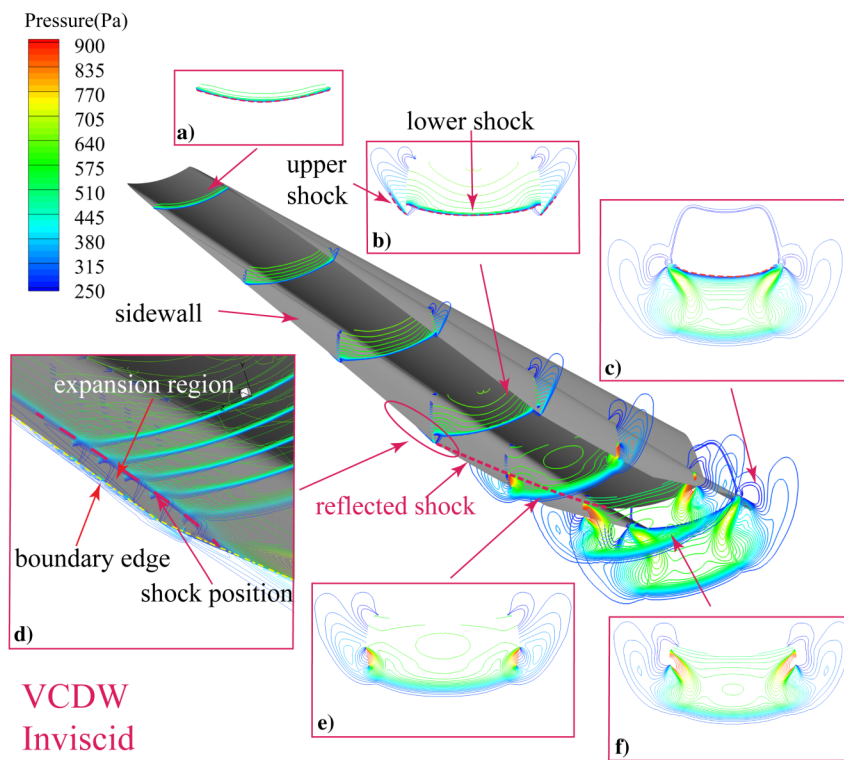


Fig. 23 Details of the inviscid pressure contour of VCDW at design condition.

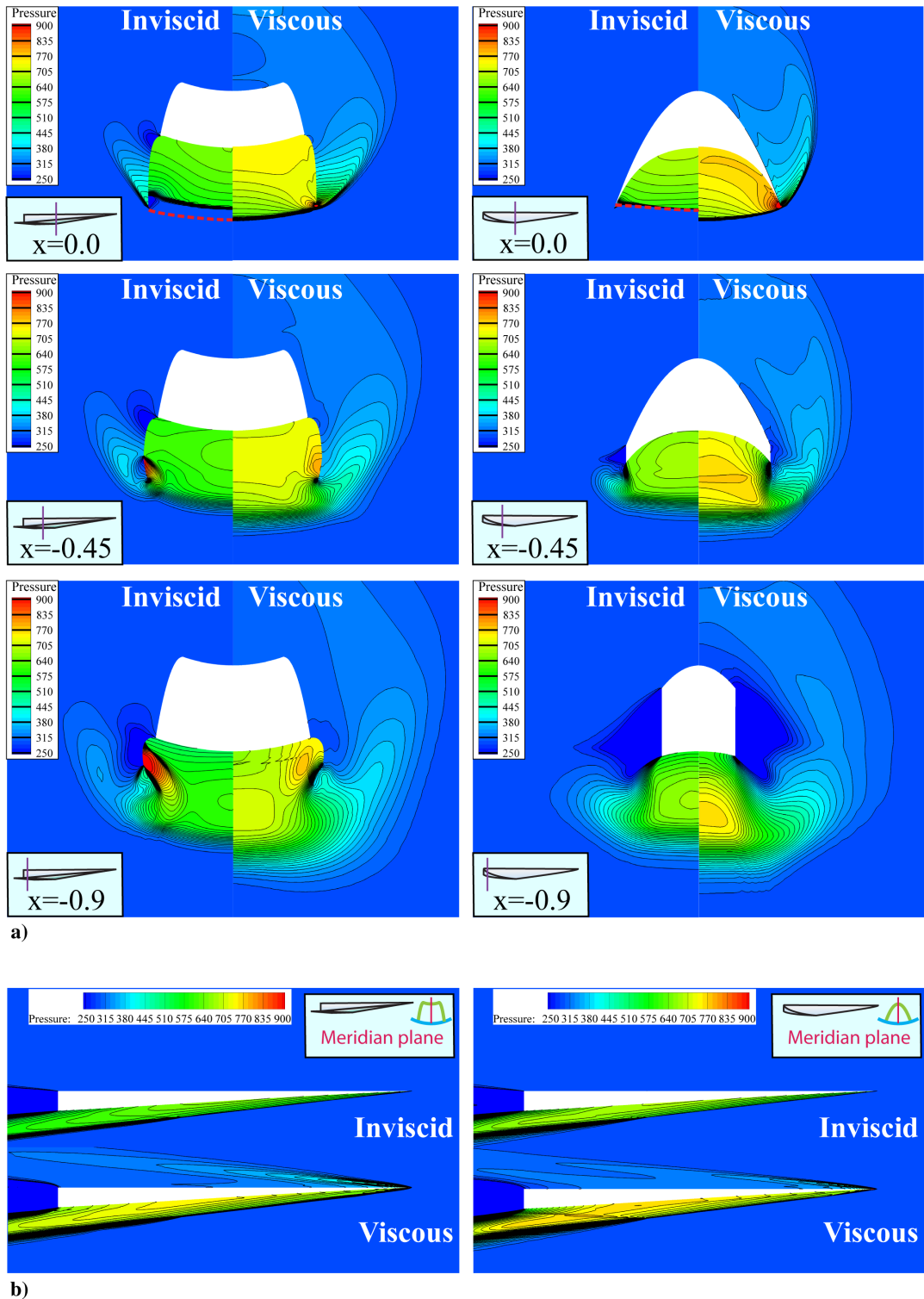


Fig. 25 Comparison of pressure contours between VCDW and CDW at design condition: a) front view of different cross sections, and b) side view of meridian plane (in units of pascals).

generation method is therefore validated. In the viscous simulation, the double-shock structure of the inviscid case transforms into a one-shock structure and the leakage of the high-pressure gas is found at both sides of the VCDW and CDW. The lower shock position of the viscous case is lower than that position of the inviscid case. In addition, the static pressure of the lower wall under the viscous condition is higher than that of the inviscid case.

C. Aerodynamic Performance Under Various Freestream Conditions

The aerodynamic performances of the VCDW, CDW, and CW2-1 are analyzed numerically under the four freestream conditions in

Table 6. The aim of this section is to prove that the VCDW has a similar aerodynamic performance under design and off-design conditions as the the CDW. Hence, four conditions are chosen for simplicity, where the flight height and flight Mach number linearly decrease. Furthermore, L/D is the main concern of this section because the Cl and Cd curves of the VCDW, CDW, and CW2-1 are remarkably similar, as shown in Fig. 26.

The comparison between the CDW and CW2-1 in Fig. 26 reflects the influence of the basic flowfield. The existence of the afterbody makes the CDW relatively more streamlined while introducing more viscous drag. The combined effects determine that the L/D of the

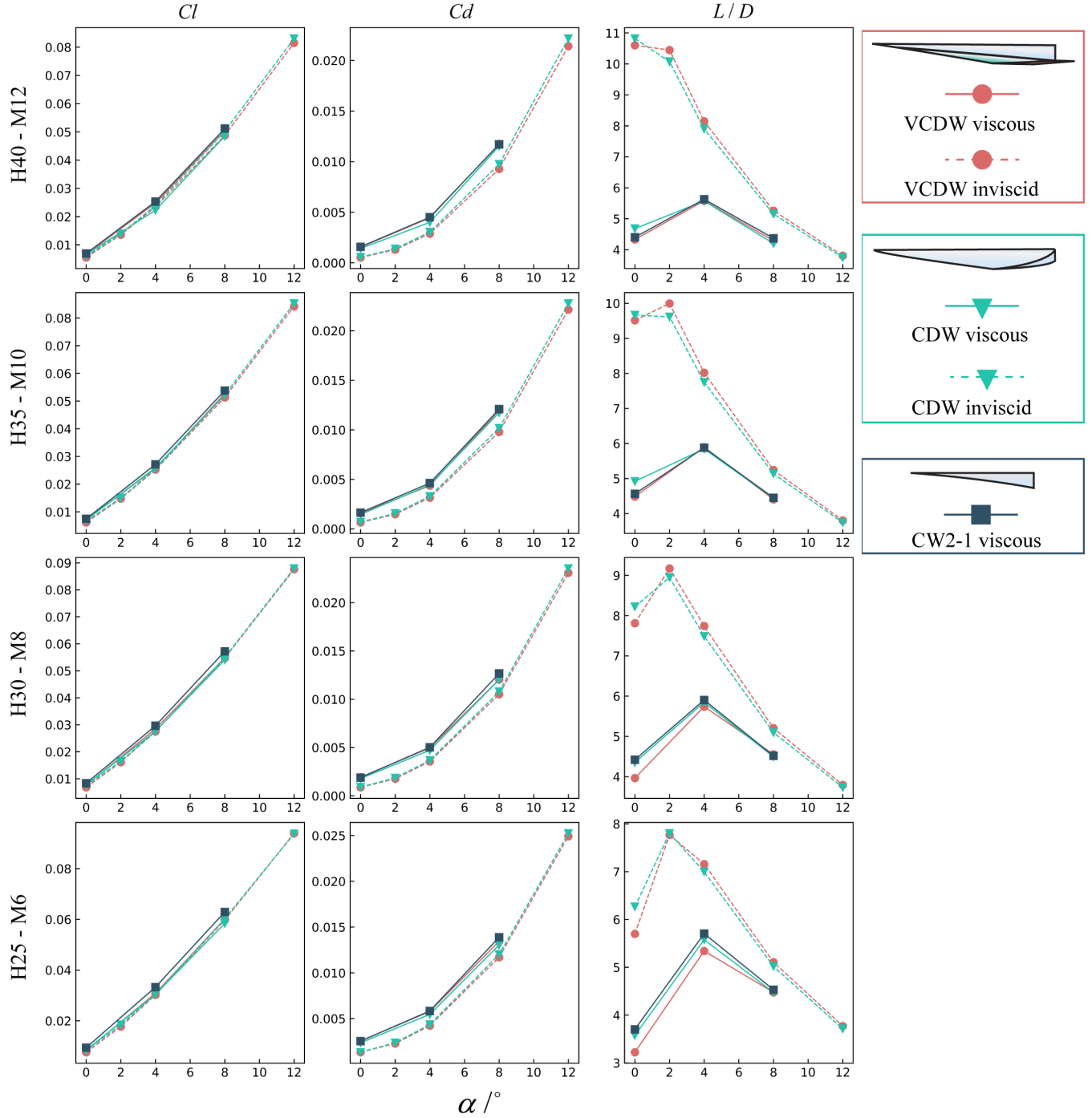


Fig. 26 Lift coefficient, drag coefficient, and lift-to-drag ratio of VCDW, CDW, and CW2-1 under various freestream conditions.

CDW is slightly larger than CW2-1 at the design condition and grows worse than CW2-1 as the freestream Mach number decreases. However, in general, extending the basic flowfield does not significantly change the aerodynamic performance of CW2-1.

The comparison between the VCDW and CDW in Fig. 26 shows that the L/D of the VCDW is slightly smaller than the CDW at the design condition due to the additional drag introduced by the upper shock and the reflected shock. The L/D gradually becomes larger than the CDW as the attack angle increases because the VCDW can capture more compressed gas. In the viscous case, the L/D of the VCDW is slightly smaller than the CDW due to a viscous effect. From the view of the FCC, the aerodynamic performance of the VCDW mainly depends on the aerodynamic performance of the main body since the sidewall is nearly vertical (which corresponds to part FD of the FCC, as shown in Fig. 5). Furthermore, the main bodies of the VCDW and CDW are generated from the same basic flowfield.

Hence, the aerodynamic performance of the VCDW and CDW are similar on the whole.

V. Conclusions

In this study, a novel volume-improved design method of large-slenderness-ratio cone-derived waveriders has been proposed, which consists of an improved basic flowfield and a specially designed M-shaped FCC. In addition, an improved evaluation method is developed to resolve the deficiency of the conventional volumetric efficiency in evaluating the space utilization, loading capacity, and upper wall expansion performance of large-slenderness-ratio waveriders. The volume performance of the proposed novel waveriders and the conventional waveriders is investigated by the proposed evaluation method, and their aerodynamic performance is analyzed by numerical simulation. According to these studies, the following conclusions can be drawn:

1) There is no significant difference in the flowfield structure and wall pressure distribution of the basic flowfield between the results of the MOC and CFD. Furthermore, no distinguishing leakage of the high-pressure gas is found in the inviscid flowfields of the forebodies of the VCDW and CDW. These results not only validate the proposed novel design method but also indicate that the proposed novel waverider can sustain good waverider characteristics.

2) In the evaluation of space utilization, the concept of an envelope box is introduced, which can reasonably describe the occupied space of the waverider. In the evaluation of loading capacity, a statistical method is introduced to quantitatively describe the loading capacity, which considers the shape of the load and the cross-sectional contour of the waverider. In the evaluation of the volume growth rate, a method is developed to simulate the process of the upper wall expansion, which can quantitatively evaluate the upper wall expansion performance.

3) The VCDW has a significant advantage over the CDW in space utilization (including nearly an 11% increment in volumetric efficiencies η_{eb-p} and η_{wet} , and a 16% increment in volume ratio $VRT_{w/eb}$), loading capacity (including nearly a 50% increment in volume ratio $VRT_{eff/eb}$, a 30% increment in volume ratio $VRT_{eff/w}$, and a 90% larger effective volume), and upper wall expansion performance (including about 3.9 times larger volume growth rate G_{exp}^V and).

4) The aerodynamic performance of the VCDW is comparable to that of the CDW. The lift coefficient Cl and drag coefficient Cd curves of the VCDW and CDW are remarkably similar under the four freestream conditions. At the design condition, the decrement of the lift-to-drag ratio from the VCDW to the CDW is less than 8%. The decrement rapidly decreases with the increasing attack of angle and leads to a similar maximum lift-to-drag ratio for the VCDW and CDW at an angle of attack of 4 deg. When the Mach number gradually deviates from the design condition, the decrement slightly increases but is still no more than 10%.

Acknowledgments

This work was supported by National Numerical Wind Tunnel Project of China (grant nos. NNW2018-ZT3B08 and NNW2019ZT7-B30).

References

- [1] McClintock, C., "X-43—Scramjet Power Breaks the Hypersonic Barrier: Dryden Lectureship in Research for 2006," *44th AIAA Aerospace Sciences Meeting and Exhibit*, AIAA Paper 2006-0001, 2006. <https://doi.org/10.2514/6.2006-1>
- [2] Hank, J., Murphy, J., and Mutzman, R., "The X-51A Scramjet Engine Flight Demonstration Program," *15th AIAA International Space Planes and Hypersonic Systems and Technologies Conference*, AIAA Paper 2008-2540, 2008. <https://doi.org/10.2514/6.2008-2540>
- [3] Spravka, J. J., and Jorris, T. R., "Current Hypersonic and Space Vehicle Flight Test Instrumentation Challenges," *AIAA Flight Testing Conference*, AIAA Paper 2015-3224, 2015. <https://doi.org/10.2514/6.2015-3224>
- [4] Pulimidi, R. R., Peace, J., Umapathy, N., Singh, M. K., Lu, F. K., and Barnard, H., "Mid-Tier Defense Against Hypersonic Glide Vehicles During Cruise," *22nd AIAA International Space Planes and Hypersonics Systems and Technologies Conference*, AIAA Paper 2018-5254, 2018. <https://doi.org/10.2514/6.2018-5254>
- [5] Yu, K., Xu, J., Gong, H., Li, R., and Liu, S., "Inverse Design Methodology of Cone-Derived Waverider Based on Pre-Defined Shock Wave Under Strong Geometric Constraints," *Acta Astronautica*, Vol. 159, June 2019, pp. 527–539. <https://doi.org/10.1016/j.actaastro.2019.02.011>
- [6] Chen, L., Deng, X., Guo, Z., Hou, Z., and Wang, W., "A Novel Approach for Design and Analysis of Volume-Improved Osculating-Cone Waveriders," *Acta Astronautica*, Vol. 161, Aug. 2019, pp. 430–445. <https://doi.org/10.1016/j.actaastro.2019.02.033>
- [7] Liu, C., Liu, Q., Bai, P., and Zhou, W., "Planform-Customized Waverider Design Integrating with Vortex Effect," *Aerospace Science and Technology*, Vol. 86, Aug. 2019, pp. 438–443. <https://doi.org/10.1016/j.ast.2019.01.029>
- [8] Zhao, Z., Huang, W., Yan, B., Yan, L., Zhang, T., and Moradi, R., "Design and High Speed Aerodynamic Performance Analysis of Vortex Lift Waverider with a Wide-Speed Range," *Acta Astronautica*, Vol. 151, Oct. 2018, pp. 848–863. <https://doi.org/10.1016/j.actaastro.2018.07.034>
- [9] Zhao, Z., Huang, W., Yan, L., Zhang, T.-T., Li, S., and Wei, F., "Low Speed Aerodynamic Performance Analysis of Vortex Lift Waveriders with a Wide-Speed Range," *Acta Astronautica*, Vol. 161, Aug. 2019, pp. 209–221. <https://doi.org/10.1016/j.actaastro.2019.05.029>
- [10] Liu, Z., Liu, J., Ding, F., Li, K., and Xia, Z., "Novel Osculating Flowfield Methodology for Hypersonic Waverider Vehicles Based on Variable Shock Angle," *Journal of Aerospace Engineering*, Vol. 31, No. 4, 2018, Paper 04018043. [https://doi.org/10.1061/\(ASCE\)AS.1943-5525.0000864](https://doi.org/10.1061/(ASCE)AS.1943-5525.0000864)
- [11] Wang, J., Liu, C., Bai, P., Cai, J., and Tian, Y., "Design Methodology of the Waverider with a Controllable Planar Shape," *Acta Astronautica*, Vol. 151, Oct. 2018, pp. 504–510. <https://doi.org/10.1016/j.actaastro.2018.06.048>
- [12] Rasmussen, M. L., "Waverider Configurations Derived from Inclined Circular and Elliptic Cones," *Journal of Spacecraft and Rockets*, Vol. 17, No. 6, 1980, pp. 537–545. <https://doi.org/10.2514/3.57771>
- [13] Sobieczky, H., Dougherty, F. C., and Jones, K., "Hypersonic Waverider Design from Given Shock Waves," *Proceedings of the First International Hypersonic Waverider Symposium*, 1990, pp. 17–19, <https://www.mendeley.com/catalogue/e7fd9ead-3cd4-3634-add6-2dbb38c9182b/>.
- [14] Sobieczky, H., Zores, B., Wang, Z., and Qian, Y. J., "High Speed Flow Design Using Osculating Axisymmetric Flows," *Proceedings of the 3rd Pacific International Conference on Aerospace Science and Technology*, 1997, pp. 182–187, <https://www.mendeley.com/catalogue/2d53c543-6799-3136-8f0b-8f7650c7dc8/>.
- [15] Rodi, P., "Geometrical Relationships for Osculating Cones and Osculating Flowfield Waveriders," *49th AIAA Aerospace Sciences Meeting Including the New Horizons Forum and Aerospace Exposition*, AIAA Paper 2011-1188, 2011. <https://doi.org/10.2514/6.2011-1188>
- [16] Rodi, P., "The Osculating Flowfield Method of Waverider Geometry Generation," *43rd AIAA Aerospace Sciences Meeting and Exhibit*, AIAA Paper 2005-0511, 2005. <https://doi.org/10.2514/6.2005-511>
- [17] Liu, Z., Liu, J., Ding, F., and Xia, Z., "Influence of Surface Pressure Distribution of Basic Flowfield on Osculating Axisymmetric Waverider," *AIAA Journal*, Vol. 57, No. 10, 2019, pp. 4560–4568. <https://doi.org/10.2514/1.J058140>
- [18] Zhang, T., Wang, Z., Huang, W., and Li, S., "A Design Approach of Wide-Speed-Range Vehicles Based on the Cone-Derived Theory," *Aerospace Science and Technology*, Vol. 71, Dec. 2017, pp. 42–51. <https://doi.org/10.1016/j.ast.2017.09.010>
- [19] Li, S., Wang, Z., Huang, W., Lei, J., and Xu, S., "Design and Investigation on Variable Mach Number Waverider for a Wide-Speed Range," *Aerospace Science and Technology*, Vol. 76, May 2018, pp. 291–302. <https://doi.org/10.1016/j.ast.2018.01.044>
- [20] Matthews, A. J., and Jones, T. V., "Design and Test of a Modular Waverider Hypersonic Intake," *Journal of Propulsion and Power*, Vol. 22, No. 4, 2006, pp. 913–920. <https://doi.org/10.2514/1.17874>
- [21] Drayna, T., Nompelis, I., and Candler, G., "Hypersonic Inward Turning Inlets: Design and Optimization," *44th AIAA Aerospace Sciences Meeting and Exhibit*, AIAA Paper 2006-0297, 2006. <https://doi.org/10.2514/6.2006-297>
- [22] Wang, X., Wang, J., and Lyu, Z., "A New Integration Method Based on the Coupling of Mutistage Osculating Cones Waverider and Busemann Inlet for Hypersonic Airbreathing Vehicles," *Acta Astronautica*, Vol. 126, Sept. 2016, pp. 424–438. <https://doi.org/10.1016/j.actaastro.2016.06.022>
- [23] Barkmeyer, D., Starkey, R., and Lewis, M., "Inverse Waverider Design for Inward Turning Inlets," *41st AIAA/ASME/SAE/ASEE Joint Propulsion Conference & Exhibit*, AIAA Paper 2005-3915, 2005. <https://doi.org/10.2514/6.2005-3915>
- [24] You, Y., Zhu, C., and Guo, J., "Dual Waverider Concept for the Integration of Hypersonic Inward-Turning Inlet and Airframe Forebody," *16th AIAA/DLR/DGLR International Space Planes and Hypersonic Systems and Technologies Conference*, AIAA Paper 2009-7421, 2009. <https://doi.org/10.2514/6.2009-7421>
- [25] Molder, S., "Internal, Axisymmetric, Conical Flow," *AIAA Journal*, Vol. 5, No. 7, 1967, pp. 1252–1255. <https://doi.org/10.2514/3.4179>

- [26] Yu, Z., Huang, G., Xia, C., and Huihui, H., "An Improved Internal-Waverider-Inlet with High External-Compression for Ramjet Engine," *20th AIAA International Space Planes and Hypersonic Systems and Technologies Conference*, AIAA Paper 2015-3612, 2015.
<https://doi.org/10.2514/6.2015-3612>
- [27] Huang, H., Huang, G., Zuo, F., and Xia, C., "Research on a Novel Internal Waverider TBCC Inlet for Ramjet Mode," *52nd AIAA/SAE/ASEE Joint Propulsion Conference*, AIAA Paper 2016-4575, 2016.
<https://doi.org/10.2514/6.2016-4575>
- [28] Ding, F., Liu, J., Shen, C.-B., Liu, Z., Chen, S.-H., and Huang, W., "Experimental Investigation of a Novel Airframe-Inlet Integrated Full-Waverider Vehicle," *AIAA Journal*, Vol. 57, No. 7, 2019, pp. 2964–2976.
<https://doi.org/10.2514/1.J058126>
- [29] Zhang, W., Liu, J., Ding, F., and Huang, W., "Novel Integration Methodology for an Inward Turning Waverider Forebody/Inlet," *Journal of Zhejiang University-Science A*, Vol. 20, No. 12, 2019, pp. 918–926.
<https://doi.org/10.1631/jzus.A1900334>
- [30] Rodi, P., "Vortex Lift Waverider Configurations," *50th AIAA Aerospace Sciences Meeting Including the New Horizons Forum and Aerospace Exposition*, AIAA Paper 2012-1238, 2012.
<https://doi.org/10.2514/6.2012-1238>
- [31] Lobbia, M. A., and Suzuki, K., "Experimental Investigation of a Mach 3.5 Waverider Designed Using Computational Fluid Dynamics," *AIAA Journal*, Vol. 53, No. 6, 2015, pp. 1590–1601.
<https://doi.org/10.2514/1.J053458>
- [32] Liu, C., Bai, P., Tian, J., and Liu, Q., "Nonlinearity Analysis of Increase in Lift of Double Swept Waverider," *AIAA Journal*, Vol. 58, No. 1, 2020, pp. 304–314.
<https://doi.org/10.2514/1.J058405>
- [33] Zheng, X., Li, Y., Zhu, C., and You, Y., "Multiple Osculating Cones' Waverider Design Method for Ruled Shock Surfaces," *AIAA Journal*, Vol. 58, No. 2, 2020, pp. 854–866.
<https://doi.org/10.2514/1.J058640>
- [34] Jiangfeng, W., Xudong, W., Jiawei, L., Tianpeng, Y., Longfei, L., and Keming, C., "Overview on Aerodynamic Design of Cruising Waverider Configuration for Hypersonic Vehicles," *Acta Aerodynamica Sinica*, Vol. 36, No. 5, 2018, pp. 7–30.
<https://doi.org/10.7638/kqdIxxb-2017.0117>
- [35] Ding, F., Liu, J., Shen, C., Liu, Z., Chen, S., and Fu, X., "An Overview of Research on Waverider Design Methodology," *Acta Astronautica*, Vol. 140, Nov. 2017, pp. 190–205.
<https://doi.org/10.1016/j.actaastro.2017.08.027>
- [36] Zucrow, M. J., and Hoffman, J. D., *Gas Dynamics*, Vol. 2, *Multidimensional Flow*, 1st ed., Wiley, New York, 1977, pp. 112–294.
- [37] Anderson, J. D., Jr., *Fundamentals of Aerodynamics*, 6th ed., Tata McGraw-Hill Education, New York, 2017, p. 624.
- [38] Ding, F., Liu, J., Shen, C., and Huang, W., "Novel Approach for Design of a Waverider Vehicle Generated from Axisymmetric Supersonic Flows Past a Pointed von Karman Ogive," *Aerospace Science and Technology*, Vol. 42, April 2015, pp. 297–308.
<https://doi.org/10.1016/j.ast.2015.01.025>
- [39] Wieting, A., and Holden, M., "Experimental Study of Shock Wave Interference Heating on a Cylindrical Leading Edge at Mach 6 and 8," *22nd Thermophysics Conference*, AIAA Paper 1978-1511, 1987.
<https://doi.org/10.2514/6.1987-1511>

S. Fu
Associate Editor